Journal of Sol-Gel Science and Technology (2022) 104:536–547
https://doi.org/10.1007/s10971-022-05887-w

INVITED PAPER: NANO-STRUCTURED MATERIALS (PARTICLES, FIBERS, COLLOIDS, COMPOSITES, ETC.)

Bottom-up synthesis of ruthenate nanosheets by aqueous solution process

Takayuki Ban[1] · Kazuki Inukai[1] · Taiki Hattori[1] · Takeshi Nagata[1] · Chika Takai-Yamashita[1] · Yutaka Ohya[1]

Received: 2 February 2022 / Accepted: 17 June 2022 / Published online: 14 July 2022

Abstract

The bottom-up synthesis of ruthenate nanosheets was examined by aqueous solution process. Upon heating mixtures of $RuCl_3$ and $N(CH_3)_4OH$ aqueous solutions at 80 °C for 1 day, highly water-dispersible ruthenate nanosheets were yielded. However, the use of RuO_2 xH_2O or $(NH_4)_2RuCl_6$ instead of $RuCl_3$ xH_2O did not produce ruthenate nanosheets. The oxidation state of ruthenium ion in the ruthenate nanosheets was +4, which inferred that the chemical composition of nanosheets is $Ru_{0.95}O_2^{0.2-}$ or $[N(CH_3)_4]_{0.2}Ru_{0.95}O_2$. Thus, the compound including Ru^{3+}, i.e., $RuCl_3$ xH_2O, was shown to be more useful for the synthesis of ruthenate nanosheets including Ru^{4+}. Probably, Ru^{3+} species played an important role in the formation of ruthenate layers. Moreover, the heating for prolonged periods or at high temperatures and the washing of ruthenate nanosheets with 2-propanol transformed some of the ruthenate nanosheets to the precipitates of layered ruthenates, which were not exfoliated in aqueous sols. It is likely that the highly water-dispersible ruthenate nanosheets are metastable states. The ruthenate nanosheets exhibited lateral sizes smaller than 100 nm and were highly dispersible in water even after the washing with 2-propanol possibly due to extensive exfoliation. Furthermore, electric properties are measured for the thin films fabricated by drying the aqueous sols of ruthenate nanosheets on a glass substrate. It is known that ruthenate nanosheets have metallic or semimetallic characters; however, the nanosheet thin films rather exhibited semiconducting properties, presumably because of poor ohmic contacts between the nanosheets.

Graphical abstract

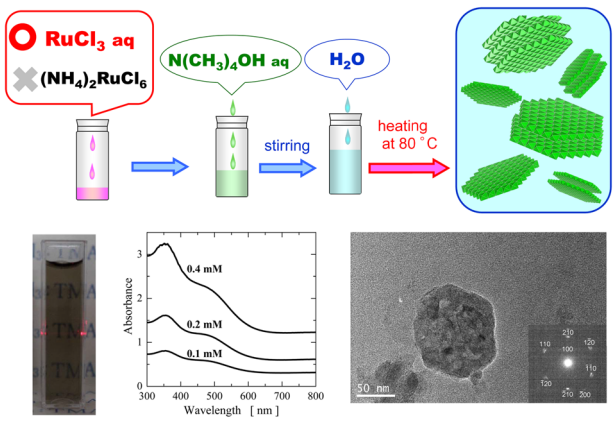

Supplementary information The online version contains supplementary material available at https://doi.org/10.1007/s10971-022-05887-w.

✉ Takayuki Ban
ban@gifu-u.ac.jp

[1] Department of Chemistry and Biomolecular Science, Gifu University, Yanagido 1-1, Gifu 501-1193, Japan

Keywords Ruthenate nanosheet · Colloidal aqueous solution · Two-dimensional material · Crystallization · Bottom-up synthesis · Layered compound

Highlights

- Ruthenate nanosheets were synthesized in aqueous sols by bottom-up process.
- Ruthenium salts including Ru^{3+} like $RuCl_3$ are useful for the formation of ruthenate nanosheets.
- Layered ruthenates with a large basal spacing were exfoliated in aqueous sols.
- The ruthenate nanosheets had lateral sizes smaller than 100 nm.

1 Introduction

Two-dimensional materials have attracted increasing attention because of interesting chemical and physical properties, which are attributed to their highly anisotropic shapes [1–4]. Metalate nanosheets are two-dimensional materials and are originated from the metalate nano-slabs in layered metalates [3–7]. They are obtained by exfoliating layered metalates. Sasaki et al. [5, 6] found that when layered metalates with bulky interlayer cations, e.g., $N(C_4H_9)_4^+$ (TBA^+), are prepared in aqueous solutions or sols, the layered metalates are swollen and exfoliated, yielding aqueous sols of metalate nanosheets. Conventionally, metalate nanosheets have been prepared by ion-exchange method [3–7]. First, the acid treatment of layered metalates leads to the replacement of interlayer cations by hydrogen ion H^+. Next, TBA^+ ion is intercalated into the interlayer by reacting the layered metalates with $N(C_4H_9)_4OH$ (TBAOH) aqueous solution, i.e., by the acid-base reaction between interlayer H^+ and TBAOH. The resulting layered metalates with interlayer TBA^+ are exfoliated, producing metalate nanosheets.

We previously found out the method for synthesizing titanate nanosheets, based on bottom-up process utilizing chemical reactions [8]. Until now, we also have synthesized other types of metalate nanosheets by the bottom-up process [9–13]. For the bottom-up synthesis, the acid-base reactions between metal hydroxides and the hydroxides of bulky cations, such as $N(CH_3)_4OH$ (TMAOH) and TBAOH, produce layered metalates with bulky interlayer cations in aqueous solutions, resulting in the formation of metalate nanosheets by the exfoliation of the obtained layered metalates. From the viewpoint of the aqueous solution chemistry relevant to the dissolution of metal hydroxide in water, the bottom-up synthesis of metalate nanosheets can be seen, as follows: Metal hydroxides with relatively strong acidity, that is, the hydroxides of the metals having large oxidation states are dissolved as metalate ions in basic aqueous solutions. However, when the hydroxides of bulky cations such as TMAOH and TBAOH are used as a pH adjuster, highly water-dispersible metalate nanosheets yield in the pH region between the precipitation of metal hydroxides and the dissolution as metalate ions because of the stabilization of anionic oligomers, i.e., metalate nanosheets, by bulky cations.

Though other researchers also have reported bottom-up syntheses of metalate nanosheets utilizing chemical reactions [14–19], the bottom-up synthesis of metalate nanosheets, which was found out by us, have some advantages. The bottom-up synthesis yields metalate nanosheets with small lateral sizes. Since small nanosheets have a large ratio of edge length to surface area, they are useful for the catalysis and photocatalysis [20, 21]. Moreover, since the metalate nanosheets are highly dispersible in water, their aqueous sols are transparent and useful as the coating sols for the fabrication of thin films by sol-gel method [22–24]. In addition, the hydrothermal treatment of the metalate nanosheet sols synthesized by the bottom-up process can yield metal oxides with interesting morphologies and crystalline phases, which cannot be obtained from other precursors [25–27]. Furthermore, this synthetic method is applicable not only to metalate nanosheets but also to metallophosphate nanosheets [28, 29]. However, most of the nanosheets synthesized so far are insulators. In order to expand the range of the applications of the metalate nanosheets, which are synthesized by bottom-up process, to a variety of functional materials, it is desirable to synthesize highly electroconductive nanosheets by this synthetic method.

Ruthenate nanosheets, e.g., $Ru_{0.95}O_2^{0.2-}$, have been synthesized by conventional ion-exchange method, that is, by replacing the interlayer cations Na^+ or K^+ in layered ruthenates, such as $K_{0.2}RuO_2$, $K_{0.2}Ru_{0.95}O_2$, $Na_{0.2}RuO_2$, and $NaRuO_2$, with TBA^+ or TMA^+ [30–38]. The resulting ruthenate nanosheets exhibited very high electric conductivity [30]. Taking advantage of their electric properties and two-dimensional morphologies, their applications to electrochemical supercapacitors [33–35], transparent conductive materials [36], the promotors for photocatalysis [37], the catalysts for oxygen evolution reactions [38, 39], and so on, have been studied extensively. So, we conceived the bottom-up synthesis of ruthenate nanosheets by reacting TMAOH or TBAOH and ruthenium hydroxide produced by hydrolyzing ruthenium salts. Since the nanosheets synthesized by the bottom-up process have small lateral sizes, they

would be useful for catalysis and photocatalysis. Moreover, resulting aqueous sols of ruthenate nanosheets also can be used as the coating sol for the thin film fabrications of ruthenates and ruthenium oxides.

The objectives of this study are to synthesize highly water-dispersible ruthenate nanosheets by bottom-up process. The ruthenium sources suitable for the bottom-up synthesis of nanosheets were also examined as well as the role of Ru^{3+} in the ruthenate nanosheet formation, the parameters influencing the dispersibility of nanosheets, and the temperature dependence of electric resistance of the thin films fabricated from resulting ruthenate nanosheets. However, since the lateral sizes of nanosheets synthesized by the bottom-up process are very small, it is hard to clarify which of monolayer nanosheets or multilayer ones are yielded. Thus, in this paper, we call not only ruthenate monolayer nanosheets but also highly water-dispersible layered ruthenates with single-nanometer thickness "ruthenate nanosheets."

2 Experimental procedure

2.1 Synthesis

The typical synthesis of ruthenate nanosheet sols by bottom-up process is as follows: Ruthenium trichloride hydrate ($RuCl_3$ xH_2O, ruthenium content of 36 to 44 mass %, FUJIFILM Wako Chemicals) (1.0 mmol) was dissolved in 3 mL of distilled water. The $RuCl_3$ aqueous solution was mixed with 25% TMAOH aqueous solution (FUJIFILM Wako chemicals, analytical grade) at a TMAOH/$RuCl_3$ molar ratio of 8. The aqueous mixture was stirred for 1 h at room temperature. Then, it was diluted with distilled water to the total volume of 10 mL, i.e., to a ruthenium concentration of 100 mM, and stirred for 1 day at room temperature. The thus-obtained aqueous sol was transferred to a closed vessel and then heat-treated at 80 °C for 1 day. The resulting aqueous sols contained highly water-dispersible ruthenate nanosheets. The uses of ruthenium (IV) oxide hydrate (RuO_2 xH_2O, Sigma-Aldrich) and ammonium hexachlororuthenate (IV) ($(NH_4)_2RuCl_6$, FUJIFILM Wako Chemicals, 99%) were also attempted instead of $RuCl_3$ xH_2O. For the use of $(NH_4)_2RuCl_6$, the ruthenium concentration was 10–50 mM and the TMAOH/Ru molar ratio was changed between 6 and 16. Since $(NH_4)_2RuCl_6$ aqueous solution is more acidic than $RuCl_3$ aqueous solution, higher TMAOH/Ru ratios were also used. Moreover, the influences of synthetic conditions, such as TMAOH/$RuCl_3$ molar ratio, heating method, heating temperature, heating period, ruthenium concentration, etc., on the synthesis of ruthenate nanosheets were also examined.

Since the aqueous sols of ruthenate nanosheets, which were synthesized using $RuCl_3$ xH_2O, contained $N(CH_3)_4Cl$ (TMACl) and excess TMAOH, the ruthenate nanosheets were washed with 2-propanol for characterization. Upon adding a copious amount of 2-propanol to the nanosheet sols, the ruthenate nanosheets were collected as precipitates. The obtained precipitates were washed several times with 2-propanol by centrifugation because TMACl and TMAOH are soluble in 2-propanol.

2.2 Characterization

X-ray diffraction (XRD) measurements were performed using a Rigaku Ultima IV diffractometer with monochromatic CuKα irradiation. The XRD patterns were recorded at 2° min^{-1} in the 2θ range of 2°–70°. For measuring XRD patterns of the colloidal particles such as nanosheets in sols, thin film samples were fabricated on a glass substrate in the following manner. A sol (100 μL) was placed all over a glass substrate (10 mm × 40 mm) by using a micropipette, and then was dried at room temperature under the ambient condition, unless otherwise stated. XRD measurements were made for the thin films fabricated on the substrates. Transmission electron microscopy (TEM) images were taken on a JEOL JEM-2100 system at an accelerating voltage of 200 kV. The samples were prepared by drying a drop of sample sol onto a Cu grid supported with a carbon-reinforced Formvar thin film (Okenshoji PVF-C15 STEM Cu150P model). The grid was subjected to hydrophilic treatment before use. Scanning electron microscopy (SEM) images were captured on a Hitachi model S-4800 at an acceleration voltage of 5 kV after coating samples with an osmium layer. Atomic force microscopic (AFM) measurements were performed on a Hitachi AFM5400L model in a tapping mode using a silicon tip cantilever (15 N m^{-1}, Hitachi SI-DF20 model). Topographic images and phase images were measured. A topographic image represents a surface profile, while a phase image represents the phase delay of cantilever tapping against input phase. Softer and more viscous surface provides larger phase delay. In this study, a phase image is useful for distinguishing ruthenate nanosheets and organic species because the former is harder than the latter. Samples for AFM measurements were prepared by dropping the aqueous sols of washed ruthenate nanosheets on a mica substrate and then drying at 100 °C for 10 min. X-ray photoelectron spectroscopy (XPS) measurements were conducted on an Ulvac-Phi Quantera-SXM model using monochromatic AlKα irradiation. A carbon tape was put on a sample holder. Then, after the vacuum deposit of a small amount of gold, sample powder was put on it. The binding energy was calibrated by adjusting Au $4f_{7/2}$ line to 84.0 eV. Thermogravimetry and differential thermal analysis (TG-DTA) were conducted on a Shimadzu DTG-60H model using about 6 mg of sample powder. TG-DTA curves were recorded in the temperature range of

25–800 °C at a heating rate of 5 °C min^{-1} under air flow of 250 mL min^{-1}, i.e., 200 mL min^{-1} of N_2 and 50 mL min^{-1} of O_2. UV–vis absorption spectra were measured on a Hitachi U-4100 model in a transmittance mode using a dual beam and were recorded in the wavelength range from 1500 to 200 nm at a rate of 300 nm min^{-1} for the sol transferred in a quartz glass cell ($10 \times 10 \times 45$ mm^3).

For the evaluation of the electric properties of ruthenate nanosheets, sheet resistivities were measured by four-probe method (Nittoseiko Analytech Loresta-GP model with a PSP type probe) for the thin films fabricated by drying the aqueous sol (100 µL) of washed ruthenate nanosheets on a glass substrate (10×40 mm^2) under the ambient condition. Moreover, the temperature dependence of the sheet resistivity of ruthenate nanosheet thin film was measured in the temperature range of 25–150 °C. The thin film was placed on a hot plate. The hot plate was set to a target temperature. After 30 min, the sheet resistivity of thin film was measured.

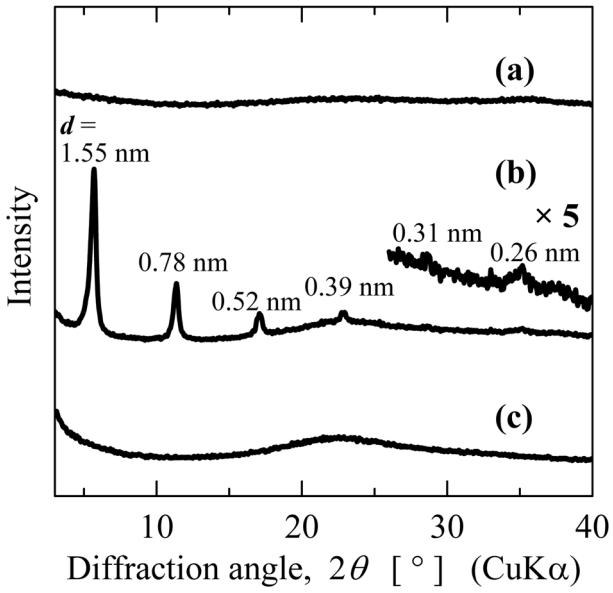

Fig. 1 XRD patterns of the samples obtained by drying the sols or suspension produced by heating aqueous mixtures of TMAOH and (**a**) RuO_2 xH_2O, (**b**) $RuCl_3$ xH_2O, or (**c**) $(NH_4)_2RuCl_6$

3 Results and discussion

3.1 Bottom-up synthesis of ruthenate nanosheets from different ruthenium salts

The bottom-up synthesis of ruthenate nanosheets was examined using different ruthenium salts such as RuO_2 xH_2O, $RuCl_3$ xH_2O and $(NH_4)_2RuCl_6$ as a ruthenium source. Each ruthenium salt was mixed with TMAOH aqueous solution in water. Then, the resulting mixtures were heated at 80 °C. First, ruthenium (IV) oxide hydrate (RuO_2 xH_2O) was used as the ruthenium source. The XRD pattern of RuO_2 xH_2O exhibited some of very broad peaks in the 2θ range of 15°–40°, suggesting very low crystallinity (Supplementary Fig. S1 in the Supplementary Information). RuO_2 xH_2O powder was mixed with TMAOH aqueous solution at a molar ratio of TMAOH/$RuO_2 = 4$, and the mixture was heated. After the heating, the powder was recovered by centrifugation. The amount of the powder was not decreased by the heating. The XRD pattern of the powder was similar to the one of the RuO_2 xH_2O powder before the heating (Fig. 1 and Supplementary Fig. S1 in the Supplementary Information). Even when the heating temperature was increased to 150 °C, the RuO_2 xH_2O powder remained intact. Thus, it was inert to basic substances.

Next, water-soluble ruthenium salts such as ruthenium (III) chloride hydrate ($RuCl_3$ xH_2O) and ammonium hexachlororuthenate (IV) ($(NH_4)_2RuCl_6$) were used because they are expected to be more reactive than inert powder RuO_2 xH_2O. The mixture of $RuCl_3$ aqueous solution and TMAOH aqueous solution with a molar ratio of TMAOH/$RuCl_3 = 8$ and a ruthenium concentration of 100 mM became blackish sols without precipitates. The thin film fabricated by drying the blackish sol under the ambient condition exhibited no XRD peaks. After heating the blackish sol at 80 °C, a thin film was also fabricated by drying the heated sol under the ambient condition. The resulting thin film provided some XRD peaks, whose *d*-spacings had a relation of 1: 1/2: 1/3: 1/4, indicating a high orientation (Fig. 1). Thus, the heating of blackish sols at 80 °C caused the colloidal particles in the sol to be crystallized to ruthenate nanosheets. The drying of the heated sol produced highly oriented ruthenates with a layered structure having $N(CH_3)_4^+$ (TMA^+) as an interlayer cation. Moreover, upon adding 2-propanol to the heated blackish sol, the colloidal particles were collected as precipitates. The powder XRD pattern of the thus-obtained precipitates provided some peaks, besides the peaks relevant to the above-mentioned high orientation. It is known that layered ruthenate Na_xRuO_2 yH_2O is in a rhombohedral system, and on the assumption of a hexagonal lattice, the ruthenate layers are parallel to the *C*-plane [33, 34]. Based on both of the lattice constant *a* of the known layered ruthenate and the lattice constant *c* estimated from the orientation peaks of the colloidal particles, all the XRD peaks of the colloidal particles were indexable (Fig. 2). Thus, this suggests that ruthenate nanosheets were synthesized in aqueous sols by the bottom-up process using $RuCl_3$ and the nanosheets had the same crystal structure as the ruthenate nanosheets reported so far [33, 34].

Ruthenate nanosheets were also attempted to be synthesized using $(NH_4)_2RuCl_6$, which is also soluble in water. An aqueous solution of $(NH_4)_2RuCl_6$ was mixed with TMAOH aqueous solution in the ratio range of TMAOH/$(NH_4)_2RuCl_6 = 6$–16. The resulting sols were heated at

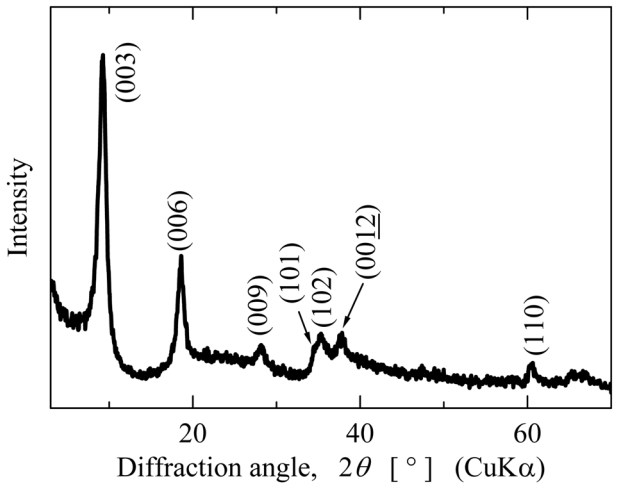

Fig. 2 XRD pattern of the precipitates obtained by adding 2-propanol to ruthenate nanosheet sols

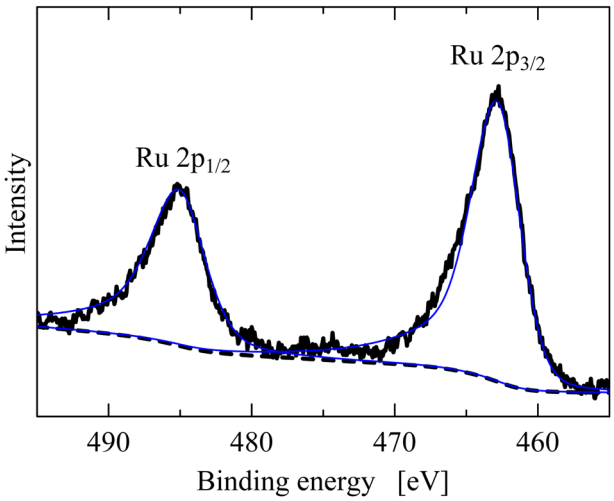

Fig. 3 XPS Ru 2p peaks of the precipitates obtained by adding 2-propanol to ruthenate nanosheet sols

80 °C, and then dried on a glass substrate under the ambient condition. The fabricated thin films exhibited no XRD peaks, indicating no formation of ruthenate nanosheets. Figure 1c shows the XRD pattern of the sample prepared at a ruthenium concentration of 50 mM and at TMAOH/$(NH_4)_2RuCl_6 = 16$. Moreover, to avoid the influence of a large amount of Cl^- ion, the precipitates obtained by adding 2-propanol to the blackish sols prepared using $(NH_4)_2RuCl_6$ were mixed with TMAOH aqueous solutions. However, ruthenate nanosheets were not yielded. Thus, even though the oxidation state of ruthenium ion in ruthenate nanosheets $Ru_{0.95}O_2^{0.2-}$, RuO_2^{x-}, or $(TMA)_{0.2}Ru_{0.95}O_2$ is equal to or close to +4, $RuCl_3$ xH_2O including Ru^{3+} was more useful for ruthenate nanosheet synthesis than $(NH_4)_2RuCl_6$ including Ru^{4+}. Zhao et al. [39] reported that the addition of $RuCl_3$ xH_2O to $NaNO_3$ melted at 350 °C yielded ruthenate (IV) nanosheets RuO_2^{x-}. Possibly, Ru^{3+} species may be useful for the formation of ruthenates with layered structures.

3.2 Oxidation of ruthenate ion during the ruthenate nanosheet synthesis using $RuCl_3$ xH_2O

As mentioned above, the oxidation state of the ruthenium ion in starting material $RuCl_3$ xH_2O is +3, while it is inferred that the synthesized ruthenate nanosheets contained Ru^{4+}. So, the oxidation of ruthenate ion during ruthenate nanosheet synthesis was examined. First, the oxidation state of ruthenium ion in ruthenate nanosheets was measured by XPS. For the precipitates obtained by adding 2-propanol to the aqueous sols of ruthenate nanosheets, XPS measurement was conducted. Since Ru 3d peaks are very close to C 1s peaks, Ru 2p peaks were observed to avoid the interference of C 1s. The peaks of Ru $2p_{1/2}$ and $_{3/2}$ appeared, and the deconvolution of their peaks showed that each of them consisted of one peak (Fig. 3). The binding energy of the Ru $2p_{3/2}$ peak was 462.9 eV, indicating the presence of Ru^{4+}, according to Ref. [40]. The XPS spectrum confirms that the oxidation state of ruthenium ion in the ruthenate nanosheets was +4.

For the bottom-up synthesis of ruthenate nanosheets, no oxidant reagents were added to the reaction sols. Probably, dissolved oxygen in the aqueous sols acted as an oxidant. The influence of dissolved oxygen was investigated by bubbling N_2 gas to the reaction sols for removing dissolved oxygen. The N_2 bubbling was started before or after the addition of TMAOH aqueous solution to $RuCl_3$ aqueous solution. Then, the mixture sols were refluxed in an oil bath at 80 °C for 1 day in N_2 atmosphere. For the thin films fabricated by drying the resulting sols on a glass substrate, XRD measurements were made. The samples without N_2 bubbling provided orientation peaks attributed to the formation of ruthenate nanosheets. Similarly, strong and sharp XRD peaks appeared in the XRD pattern of the sample with N_2 bubbling after TMAOH addition (Supplementary Fig. S2 in the Supplementary Information). However, for the sample with the start of N_2 bubbling before TMAOH addition, the XRD peaks became weaker and broader (Supplementary Fig. S2 in the Supplementary Information). Thus, this suggests that the oxidation of Ru^{3+} with dissolved oxygen occurred rapidly in basic aqueous sols and influenced the crystallization of ruthenate nanosheets.

3.3 Influence of synthetic conditions on the bottom-up synthesis of ruthenate nanosheets from $RuCl_3$ xH_2O

The influence of different synthetic conditions on the bottom-up synthesis of ruthenate nanosheets from $RuCl_3$ xH_2O was investigated. First, TMAOH/$RuCl_3$ molar ratio was changed from 3 to 8, while the ruthenium concentration was fixed to

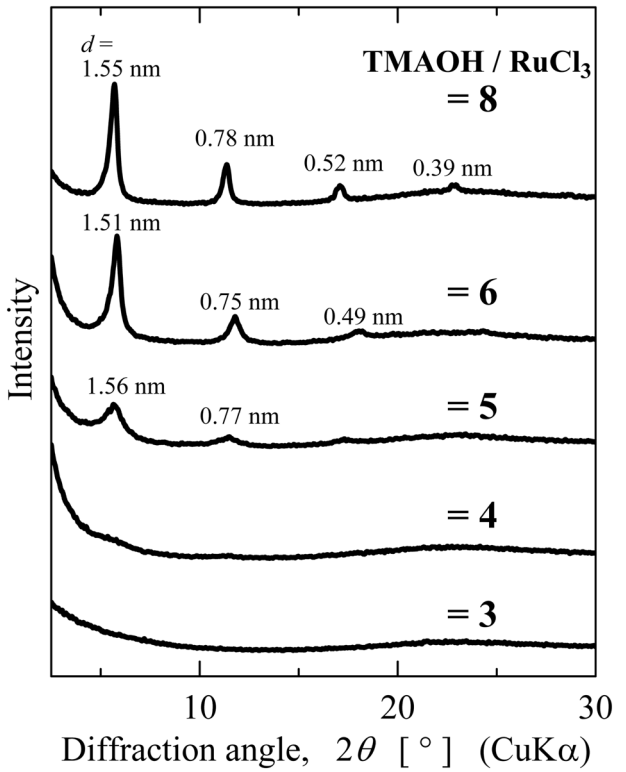

Fig. 4 XRD patterns of the thin films fabricated by drying the sols, which were prepared by heating the aqueous mixtures of TMAOH and $RuCl_3$ at different TMAOH/$RuCl_3$ ratios

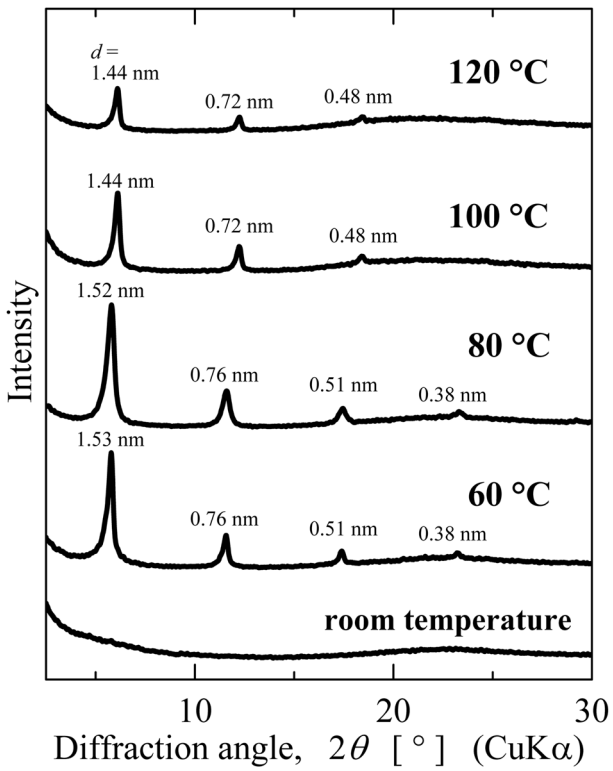

Fig. 5 XRD patterns of the thin films fabricated by drying the sols, which were prepared by heating the aqueous mixtures of TMAOH and $RuCl_3$ at different temperatures

100 mM. At TMAOH/$RuCl_3$ = 3, the pH of sol was 5.4, while at TMAOH/$RuCl_3$ ≥4, the pH values were increased to pH ≥ 12.9. XRD measurements were conducted for the thin films fabricated by drying the heated sols (Fig. 4). At TMAOH/$RuCl_3$ = 3 and 4, the thin films exhibited no XRD peaks. At TMAOH/$RuCl_3$ ≥ 5, the orientation peaks attributed to ruthenate nanosheet formation appeared. The intensities of the peaks were increased with TMAOH/$RuCl_3$ ratios and leveled off at TMAOH/$RuCl_3$ = 8. Thus, strongly basic sols were required for the bottom-up synthesis of ruthenate nanosheets.

Next, the influence of $RuCl_3$ concentration was investigated. The $RuCl_3$ concentration was decreased from 100 mM to 20 mM at TMAOH/$RuCl_3$ = 8. The thin films were fabricated by drying the sols on a glass substrate ($10 \times 40\ mm^2$) at the fixed Ru amount of 5 μmol. In the XRD patterns of the thin films, the orientation peaks became weaker with decreasing $RuCl_3$ concentration (Supplementary Fig. S3 in the Supplementary Information). High Ru^{n+} concentration was preferable for ruthenate nanosheet formation. Moreover, since ruthenate nanosheet sols were synthesized by heating the aqueous mixtures of $RuCl_3$ and TMAOH, the influence of heating temperature and periods were also investigated. The heating temperature was changed from room temperature (without heating) to 120 °C (Fig. 5). When the mixture sol was not heated, no ruthenate nanosheets was yielded. At heating temperatures higher than 60 °C, ruthenate nanosheets were yielded. The amount of formed nanosheets was maximum at 80 °C. Furthermore, the heating period was changed from 1 day to 7 days at 80 °C (Supplementary Fig. S4 in the Supplementary Information). The prolonged heating for periods longer than 1 day decreased the amount of ruthenate nanosheets. For the sols heated at high temperatures (≥100 °C) or for long periods (≥4 days), small amounts of precipitates were formed. XRD measurement shows that the precipitates were also layered ruthenates (Supplementary Fig. S5 in the Supplementary Information). The layered ruthenates formed by drying the ruthenate nanosheet sols had a basal spacing of 1.45–1.56 nm, while the basal spacing of the precipitates was about 0.95 nm. Thus, these results suggest that the ruthenate nanosheets highly dispersed in water are metastable, and the heating at high temperatures for a long period transforms some ruthenate nanosheets into stable layered ruthenates, which have small basal spacing and are not dispersible in water.

3.4 Characterization of the ruthenate nanosheets

UV–vis measurements were made for aqueous sols of ruthenate nanosheets. The ruthenate nanosheet sols

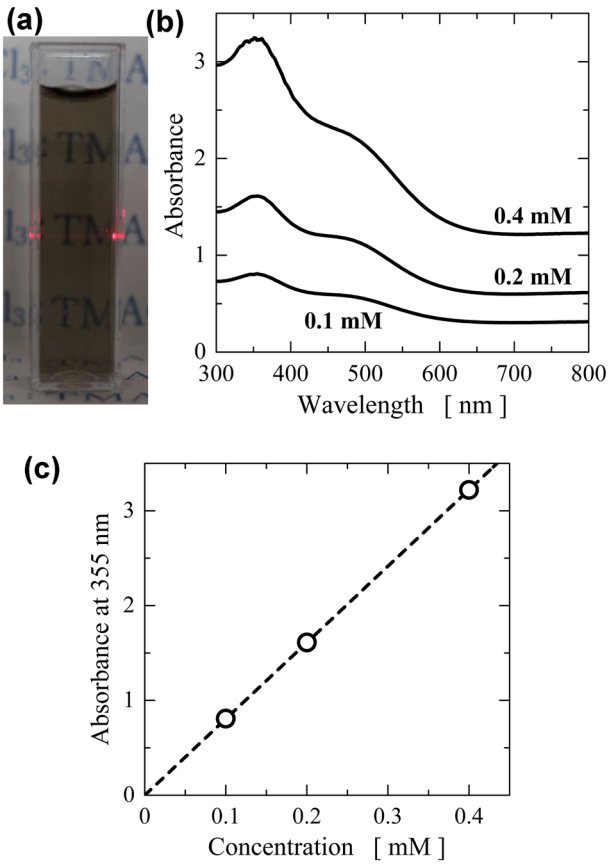

Fig. 6 (**a**) Appearance and (**b**) UV–vis spectra of the diluted sols of ruthenate nanosheets and (**c**) the dependence of the absorbance at 355 nm on the concentrations of the sols

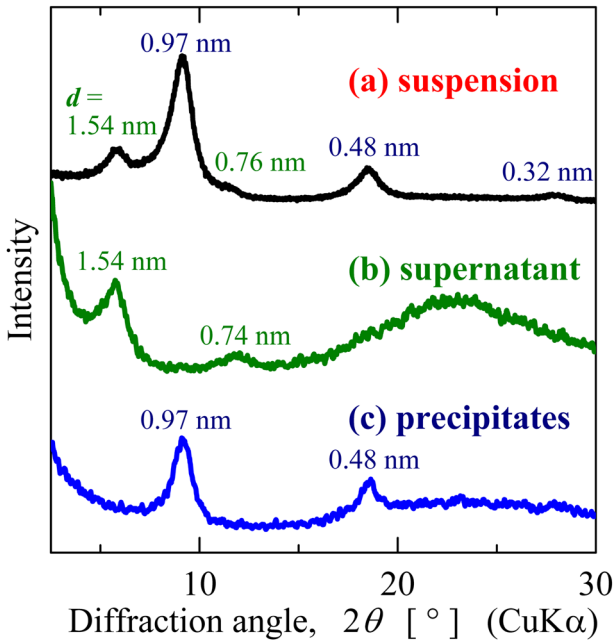

Fig. 7 XRD patterns of the samples obtained (**a**) by drying the aqueous suspension of the precipitates obtained by adding 2-propanol to ruthenate nanosheet sols and (**b**) by drying the supernatant of the aqueous suspension, and XRD pattern of the precipitates in the aqueous suspension

synthesized by heating a starting sol with a composition of $TMAOH/RuCl_3 = 8$ and a ruthenium concentration of 100 mM at 80 °C for 1 day were diluted to concentrations of 0.1–0.4 mM with distilled water. The nanosheet sol with a concentration of 0.1 mM (Fig. 6a) was blackish and transparent with no precipitates. Upon irradiating a laser light to the aqueous sol, the trace of the light passage was observed due to Tyndall effect. Moreover, the UV–vis spectra exhibited absorption peaks around 355 nm and 500 nm (Fig. 6b). Similar UV–vis spectra were already reported for the aqueous sols of ruthenate nanosheets $Ru_{0.95}O_2^{0.2-}$ [41] and $RuO_2^{0.2-}$ [34] and for the thin films of layered ruthenate consisting of ruthenate nanosheets $RuO_{2.1}^{0.2-}$ and TBA^+ [30]. The UV–vis spectra confirmed that the ruthenate nanosheets synthesized in this study were similar in crystal structure to those synthesized by the conventional method. Furthermore, the absorbance of the peak at 355 nm was proportional to the ruthenium concentration of the aqueous sols (Fig. 6c), suggesting that the ruthenate nanosheets were highly dispersed due to extensive exfoliation. The molar extinction coefficient of the absorption peak at 355 nm was estimated as $8.06 \times 10^3\ mol^{-1}\ dm^3\ cm^{-1}$. It was a little larger than the one reported for the ruthenate nanosheet sols synthesized by the conventional method [34]. It is likely that the difference in molar extinction coefficient is attributed to the size of ruthenate nanosheets.

Since the ruthenate nanosheet sols also contained TMACl and excess TMAOH, the nanosheets were collected as precipitates by adding 2-propanol to the sols and washed several times with 2-propanol by centrifugation. When the precipitates were added to water again, parts of the precipitates were highly dispersed in water; however, the other parts remained intact as precipitates. The XRD pattern (Fig. 7a) of the aqueous suspension exhibited two types of layered ruthenates; one had a basal spacing of 1.54 nm, while the basal spacing of the other was 0.97 nm. So, the suspension was separated into supernatant and precipitates. Upon drying the supernatant under the ambient condition, layered ruthenates were formed with a basal spacing around 1.54 nm (Fig. 7b), indicating the presence of highly dispersible ruthenate nanosheets in the supernatant. On the other hand, the precipitates were layered ruthenates with a basal spacing of 0.97 nm (Fig. 7c), indicating that they were the above-mentioned stable layered ruthenate. Thus, the washing with 2-propanol transformed some of highly water-dispersible ruthenate nanosheets to the stable layered ruthenates which were not dispersible in water.

In order to investigate the state of TMA^+ in layered ruthenates, thermal analysis was performed for the layered ruthenates obtained by washing with 2-propanol. First, TG-

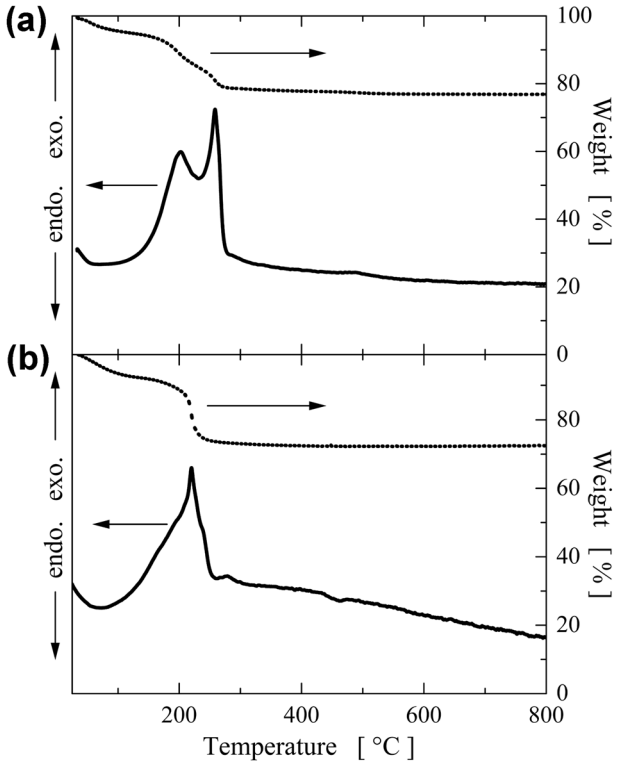

Fig. 8 TG-DTA curves of the layered ruthenate precipitates obtained (**a**) by the washing of ruthenate nanosheets with 2-propanol and (**b**) by the washing them with 2-propanol and water

DTA measurement was made for the precipitates of layered ruthenates before the re-dispersion in water (Fig. 8a). At temperatures lower than 120 °C, the desorption of adsorbed water was observed. Around 200 °C and 270 °C, two exothermic peaks appeared accompanying weight losses, which were assignable to the combustion of TMA^+ species. The precipitates heated at 800 °C were RuO_2. Based on the observed weight losses, the TMA^+/Ru ratio was estimated to be about 0.33. Next, TG-DTA measurement was also conducted for the precipitates obtained after the re-dispersion in water (Fig. 8b). The exothermic peaks accompanying weight losses were observed at 200 °C. The weight losses showed that the TMA^+/Ru ratio was about 0.33. Thus, the removal of highly dispersible ruthenate nanosheets disappeared the exothermic peak at 270 °C. The exfoliation and dispersibility of layered ruthenate depended on the state of interlayer TMA^+. TMA^+ species providing the exothermic combustion peak at 270 °C had some relevance to water-dispersible ruthenate nanosheets. Moreover, the chemical composition of the ruthenate nanosheets reported so far, e.g., $[Ru^{IV}_{0.95}O_2]^{0.2-}$, corresponds to the TMA^+/Ru ratio of 0.2. However, the TG-DTA curves showed the TMA^+/Ru ratio of about 0.33. It is likely that the layered ruthenate powders synthesized by bottom-up process contained excess TMAOH.

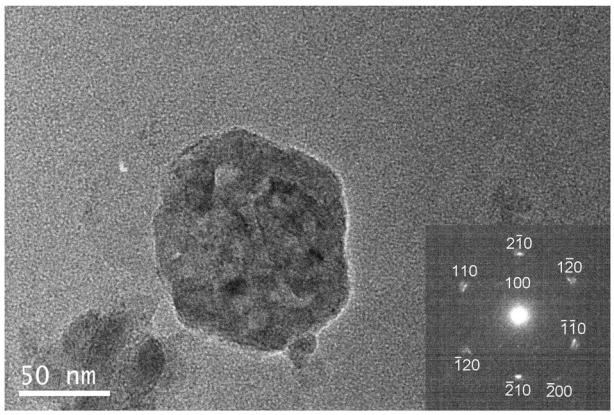

Fig. 9 TEM image and SAED pattern of the aggregate of the highly-water dispersible ruthenate nanosheets obtained by washing with 2-propanol and subsequential dispersion in water

Next, the morphology of ruthenate nanosheets was examined. For the ruthenate nanosheets, which were dispersible in water even after the washing with 2-propanol, TEM observation was conducted. In the TEM images, lots of ruthenate nanosheets were present with lateral sizes smaller than 100 nm. Thus, the highly water-dispersible ruthenate nanosheets were very small. As shown in Fig. 9, the aggregates of ruthenate nanosheets were also seen. The aggregate shown in Fig. 9 had a lateral size of about 100 nm and a shape like a hexagon surrounded with the {100} planes, although it was an aggregate. Moreover, it exhibited an SAED pattern like that of a hexagonal single crystal, although the diffraction spots were a little diffused. The SAED spots were assignable using the lattice constant *a* of the known layered ruthenate, confirming that the crystals in the aggregate were ruthenate nanosheets or layered ruthenates.

For the ruthenate nanosheets after the washing with 2-propanol, AFM observation was conducted in a tapping mode (Fig. 10). Topographic image (Fig. 10a) and phase image (Fig. 10c) were measured. A topographic image shows the surface profile, while a phase image shows the phase delay of cantilever tapping against an input phase. Softer and more viscous surface provides larger phase delay, that is, lighter yellow colors in a phase image (Fig. 10c), while hard surface provides darker brown because of small phase delay. In this study, a phase image was measured for distinguishing ruthenate nanosheets and organic species because the former is harder than the latter. In the topographic image, many small sheet-like particles were seen (Fig. 10a). They were as small as 20–50 nm in lateral size and were about 1 nm thick (Fig. 10b). In the phase image, the phases on the particles were similar to those on the mica substrate surface (Fig. 10c). Moreover, the phase images were analyzed in more detail. The cantilever was scanned from the left side to the right one in Fig. 10c, d.

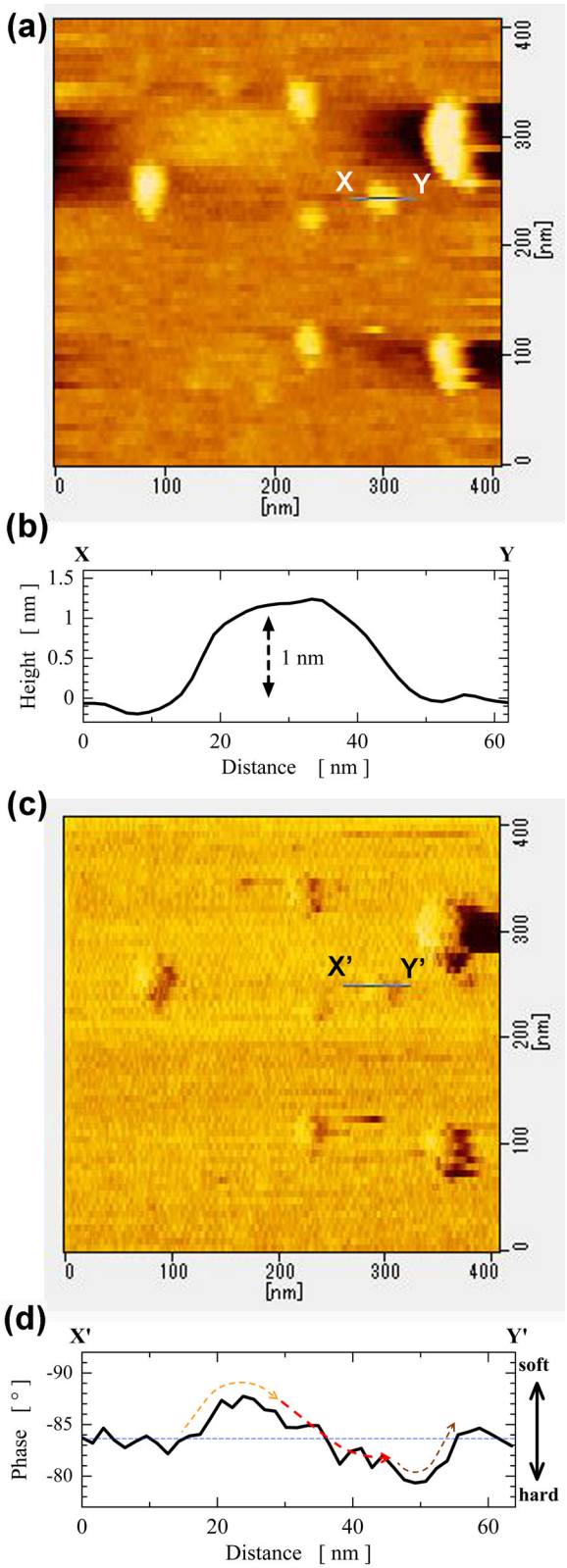

Fig. 10 (**a**) Topographic image and (**c**) phase image of AFM measurement for the highly-water dispersible ruthenate nanosheets obtained by washing with 2-propanol and subsequential dispersion in water. The panels **b** and **d** show the height profile along the line of X to Y in **a** and the phase profile along the line of X' to Y' in **c**, respectively

When the cantilever reached sheet-like particles, the phase delay was increased a little at the edge of 1-nm thick particle (Fig. 10d) because a force parallel to the sample surface was applied to the cantilever due to the change in height. At the right edge of sheet-like particles, the phase delay was decreased a little because of the same reason as the left-side edge of particles. As a result, the left side of particles became light yellow, whereas the right side was dark brown. The phase delay in the center of sheet-like particles corresponds to the hardness of the particles. The phase delay of tapping was similar to that of the surface of mica substrate and gradually decreased as the cantilever proceeded, meaning that the hardness of the surfaces of the particles was similar to or a little larger than that of the mica substrate surface. In addition, some sheet-like particles with a thickness of about 2 nm were also seen (Supplementary Fig. S7 in the Supplementary Information). Similar AFM results were also obtained for them. The left sides of the particles were light yellow, while the right side was dark brown. However, the areas without the influence of the edges were wider for 2-nm thick particles than for the 1-nm thick ones. The middle of the 2-nm thick particles was a little harder than the mica substrate surface. The gradual phase change on the 1-nm thick particles was probably attributed to the small thickness. The particles were so thin that the hardness of particle surface gradually influenced the phase of cantilever tapping. These results suggest that the sheet-like particles were ruthenate nanosheets, but not lumps of organic species. It is likely that the 1-nm thick particles and 2-nm thick ones were monolayer ruthenate nanosheets and bilayer nanosheets, respectively.

TEM and AFM images suggest the presence of some types of ruthenate nanosheets, i.e., monolayer, bilayer, and multilayer nanosheets and the aggregates of nanosheets, in the highly water-dispersible ruthenate nanosheets. Furthermore, SEM observation was conducted for the layered ruthenates which were not dispersible in water (Fig. 11). The layered ruthenates were particles with sizes of 100–200 nm. Thus, there was difference in lateral size between highly dispersible ruthenate nanosheets and layered ruthenate precipitates.

3.5 Electric properties of ruthenate nanosheets

Thin films were fabricated using aqueous sols of the ruthenate nanosheets, which were dispersible in water even after the washing with 2-propanol. The sol was dried on a glass substrate under the ambient condition. The sheet resistivity of the resulting thin film was measured by four-probe method. It was about 400 kΩ sq^{-1}. Although Sato et al. [28] reported as low sheet resistivity as 12 kΩ sq^{-1} for single ruthenate nanosheet, which was measured by scanning probe microscopy; the sheet resistivity measured in

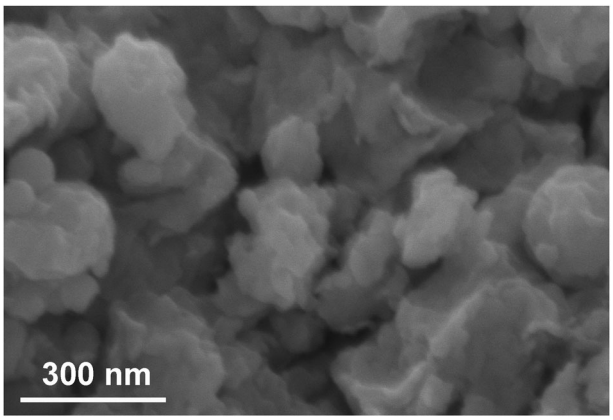

Fig. 11 SEM image of the layered ruthenate precipitates obtained by washing with 2-propanol and subsequential dispersion in water

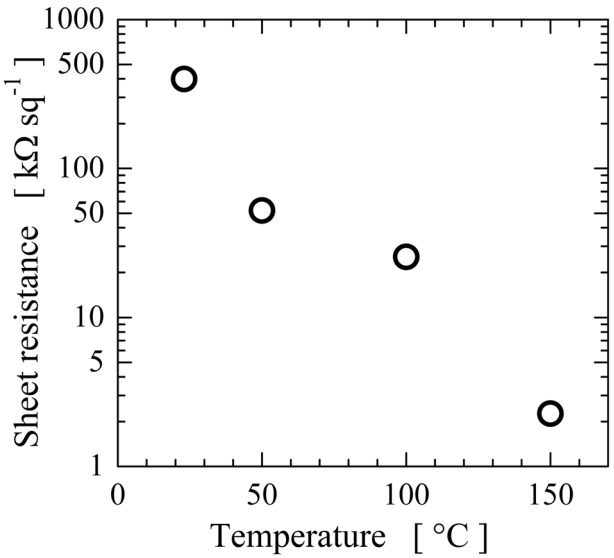

Fig. 12 Change of the sheet resistance of ruthenate nanosheet thin film with temperature. The thin film was fabricated from the highly-water dispersible ruthenate nanosheets obtained by washing with 2-propanol and subsequential dispersion in water

this study was not so low because of the small lateral size of ruthenate nanosheets, that is, the presence of lots of interfaces between nanosheets. Furthermore, the temperature dependence of the sheet resistivity of the ruthenate nanosheet thin film was investigated (Fig. 12). The sheet resistivity was decreased with increasing temperature, suggesting that the thin films of ruthenate nanosheets had the semiconductive characters of electric conduction. However, it is known that ruthenate nanosheets exhibit metallic or semimetallic conductivity [42]. Since the ruthenate nanosheets synthesized in this study had very small lateral sizes, the interfaces between ruthenate nanosheets have a significant influence on the electric conductivity. It is likely that the interfaces provided poor ohmic contacts between ruthenate nanosheets, thereby the ruthenate nanosheet thin film exhibited rather semiconductivity.

4 Conclusions

Ruthenate nanosheets were synthesized by bottom-up process in aqueous solutions. Upon heating the aqueous mixtures of $RuCl_3$ solutions and TMAOH solutions at 80 °C for 1 day yielded ruthenate nanosheets. Since the bottom-up synthesis produced highly water-dispersible nanosheets, the resulting sols can be used as the coating sols for the thin film fabrication by sol-gel method. Moreover, even though the oxidation state of ruthenium ion in the ruthenate nanosheets was +4, $RuCl_3$ xH_2O including Ru^{3+} ion was more useful as the ruthenium source of ruthenate nanosheets than RuO_2 xH_2O and $(NH_4)_2RuCl_6$, which include Ru^{4+}. The oxidation of Ru^{3+} to Ru^{4+} with dissolved oxygen occurred spontaneously in strongly basic aqueous solutions during the bottom-up process. For the synthesis of ruthenate nanosheets by the conventional ion-exchange method, some research groups reported the use of layered potassium ruthenate $K_{0.2}Ru_{0.95}O_2$ powder as a starting material. However, for the solid-state synthesis of $K_{0.2}Ru_{0.95}O_2$ from K_2CO_3 and RuO_2, excess K_2CO_3 (K_2CO_3:$RuO_2 = 5:8$) and the firing at a temperature as high as 850 °C are required [30, 31, 33, 36], indicating low reactivities of Ru^{4+} species. On the other hand, it was reported that the addition of $RuCl_3$ xH_2O to $NaNO_3$ melted at 350 °C produced ruthenate nanosheets [39]. Probably, Ru^{3+} species plays an important role in the formation of ruthenate layers. Furthermore, two types of layered ruthenates with bulky interlayer cation TBA^+ were reported so far: One has as large a basal spacing as 1.65 nm [33, 34]. The other has a relatively small basal spacing, which was 1.28 nm [31, 36]. In this study, the stacking of highly water-dispersible ruthenate nanosheets involving TMA^+ provided layered ruthenates with a basal spacing as large as about 1.5 nm, while the layered ruthenates with relatively small basal spacings around 0.95 nm were yielded as precipitates by the heating for prolonged periods or at high temperatures. Thus, two types of basal spacings were also observed for layered ruthenates with TMA^+. The layered ruthenate with smaller basal spacing was more stable, while the layered ruthenate with larger basal spacing was metastable and highly dispersible in water, producing ruthenate nanosheets. The highly water-dispersible ruthenate nanosheets were smaller than 100 nm in lateral size.

Until now, we have reported the bottom-up syntheses of metalate nanosheets and metallophosphate nanosheets by aqueous solution process. However, many of them were insulators. In this study, ruthenate nanosheets, which showed semiconductive properties, were synthesized by the

bottom-up method. The extension of the properties of obtainable metalate nanosheets would widen the range of their applications to functional nanomaterials.

Acknowledgements This study was supported by KAKENHI (Grant-in-Aid for Scientific Research 21K05225) from Japan Society for the Promotion of Science (JSPS). We thank Dr. Michiyuki Yoshida in Gifu University for helping with TEM measurements.

Funding This study was supported by KAKENHI (Grant-in-Aid for Scientific Research 21K05225) from Japan Society for the Promotion of Science (JSPS).

Compliance with ethical standards

Conflict of interest The authors declare no competing interests.

Publisher's note Springer Nature remains neutral with regard to jurisdictional claims in published maps and institutional affiliations.

References

1. Huang X, Tan C, Yin Z, Zhang H (2014) 25th anniversary article: hybrid nanostructures based on two-dimensional nanomaterials. Adv Mater 26:2185–2204
2. Ma R, Sasaki T (2010) Nanosheets of oxides and hydroxides: ultimate 2D charge-bearing functional crystallites. Adv Mater 22:5082–5104
3. Osada M, Sasaki T (2012) Two-dimensional dielectric nanosheets: novel nanoelectronics from nanocrystal building blocks. Adv Mater 24:210–228
4. Wang TH, Henderson CN, Draskovic TI, Mallouk TE (2014) Synthesis, exfoliation, and electronic/protonic conductivity of the dion–jacobson phase layer perovskite $HLa_2TiTa_2O_{10}$. Chem Mater 26:898–906
5. Sasaki T, Watanabe M, Hashizume H, Yamada H, Nakagawa H (1996) Macromolecule-like aspects for a colloidal suspension of an exfoliated titanate. pairwise association of nanosheets and dynamic reassembling process initiated from it. J Am Chem Soc 118:8329–8335
6. Sasaki T, Watanabe M, Hashizume H, Yamada H, Nakagawa H (1996) Reassembling process of colloidal single-layers of an exfoliated titanate. Chem Commun 229–230. https://doi.org/10.1039/CC9960000229.
7. Schaak RE, Mallouk TE (2000) Prying apart ruddlesden−popper phases: exfoliation into sheets and nanotubes for assembly of perovskite thin films. Chem Mater 12:3427–3434
8. Ohya T, Nakayama A, Ban T, Ohya Y, Takahashi Y (2002) Synthesis and characterization of halogen-free, transparent, aqueous colloidal titanate solutions from titanium alkoxide. Chem Mater 14:3082–3089
9. Ban T, Yoshikawa S, Ohya Y (2011) Synthesis of transparent aqueous sols of colloidal layered niobate nanocrystals at room temperature. J Colloid Inter Sci 364:85–91
10. Ban T, Yoshikawa S, Ohya Y (2012) Synthesis of layered tantalate nanocrystals by aqueous process at room temperature. CrystEngComm 14:7709–7714
11. Ban T, Ito T, Ohya Y (2013) Phase transition between layered tungstates and polyoxotungstates in aqueous solutions. Inorg Chem 52:10520–10524
12. Ban T, Wakita T, Yokoyama R, Miyake T, Ohya Y (2018) Influence of the negative charge density of metalate nanosheets on their bottom-up synthesis. CrystEngComm 20:3559–3568
13. Ban T, Kaiden T, Ohya Y (2019) Hydrothermal synthesis of layered perovskite-structured metal oxides and cesium tungstate nanosheets. Cryst Growth Des 19:6903–6910
14. Chemseddine A, Moritz T (1999) Nanostructuring titania: control over nanocrystal structure, size, shape, and organization. Eur J Inorg Chem 1999:235–245
15. Nakamura K, Oaki Y, Imai H (2013) Monolayered nanodots of transition metal oxides. J Am Chem Soc 135:4501–4508
16. Tae EL, Lee KE, Jeong LS, Yoon KB (2008) Synthesis of diamond-shape titanate molecular sheets with different sizes and realization of quantum confinement effect during dimensionality reduction from two to zero. J Am Chem Soc 130:6534–6543
17. Kai K, Yoshida Y, Kageyama H, Saito G, Ishigaki T, Furukawa Y, Kawamata J (2008) Room-temperature synthesis of manganese oxide monosheets. J Am Chem Soc 130:15938–15943
18. Lin C-H, Wong DS-H, Lu S-Y (2014) Layered protonated titanate nanosheets synthesized with a simple one-step, low-temperature, urea-modulated method as an effective pollutant adsorbent. ACS Appl Mater Interfaces 6:16669–16678
19. Portehault D, Giordano C, Sanchez C, Antonietti M (2010) Nonaqueous route toward a nanostructured hybrid titanate. Chem Mater 22:2125–2131
20. Ban T, Kondoh S, Ohya T, Ohya Y, Takahashi Y (2003) Photocatalysis of a transparent titanate aqueous sol prepared from titanium tetraisopropoxide and tetramethylammonium hydroxide. J Photochem Photobio A Chem 156:219–225
21. Ban T, Yamada H, Imaeda K, Inoue K, Takai C, Ohya Y (2020) Light absorption and photocatalysis of flake-like titanate nanosheets chemically modified by organic ligands. J Ceram Soc Jpn 128:890–897
22. Ban T, Ito T, Ohya Y (2013) Orientation of tungsten trioxide thin films fabricated by sol-gel method using aqueous sols of colloidal layered tungstates. J Sol Gel Sci Technol 68:88–94
23. Ohya T, Nakayama A, Ban T, Ohya Y, Takahashi Y (2003) Effect of photoirradiation on the properties of layered titanate thin films from transparent aqueous titanate sols. Bull Chem Soc Jpn 76:429–435
24. Ohya T, Nakayama A, Shibata Y, Ban T, Ohya Y, Takahashi Y (2003) J Sol Gel Sci Technol 26:799–802
25. Ban T, Nakatani T, Uehara Y, Ohya Y (2008) Microstructure of six-pointed starlike anatase aggregates. Cryst Growth Des 8:935–940
26. Ban T, Tanaka Y, Ohya Y (2011) Hydrothermal synthesis of highly water-dispersible anatase nanocrystals from transparent aqueous sols of titanate colloids. J Nanopart Res 13:273–281
27. Ban T, Hamajima A, Akao N, Takai-Yamashita C, Ohya Y (2021) Hydrothermal synthesis of highly pure brookite-type titanium oxide powder from aqueous sols of titanate nanosheets. Adv Powder Technol 32:3601–3609
28. Ban T, Asano K, Takai-Yamashita C, Ohya Y (2020) Bottom-up synthesis of titanophosphate nanosheets by the aqueous solution process. Nanoscale Adv 2:3542–3549
29. Ban T, Iriyama S, Ohya Y (2018) Bottom-up synthesis of aluminophosphate nanosheets by hydrothermal process. Adv Powder Technol 29:537–542
30. Sato J, Kato H, Kimura M, Fukuda K, Sugimoto W (2010) Conductivity of ruthenate nanosheets prepared via electrostatic self-assembly: characterization of isolated single nanosheet crystallite to mono- and multilayer electrodes. Langmuir 26:18049–18054
31. Kim SY, Shin WH, Jung DW, Ko D-S, Roh JW, Hwang S, Lee J, Lee K, Park HJ, Kwak C, Kim S-I, Jeong HM, Lee KH, Kim HS (2020) Facile and accelerated production of RuO2monolayersviaa dual-step intercalation process. Inorg Chem Front 7:1445–1450

32. Shikano M, Delmas C, Darriet J (2004) $NaRuO_2$ and $NaxRuO_2{\cdot}yH_2O$: new oxide and oxyhydrate with two dimensional RuO2layers. Inorg Chem 43:1214–1216
33. Sugimoto W, Iwata H, Yasunaga Y, Murakami Y, Takasu Y (2003) Preparation of ruthenic acid nanosheets and utilization of its interlayer surface for electrochemical energy storage. Angew Chem Int Ed 42:4092–4096
34. Fukuda K, Saida T, Sato J, Yonezawa M, Takasu Y, Sugimoto W (2010) Synthesis of nanosheet crystallites of ruthenate with an α-$NaFeO_2$-related structure and its electrochemical supercapacitor property. Inorg Chem 49:4391–4393
35. Vijayabara V, Senthilkumar N, Nehru K, Karvembu R (2018) Hydrothermal synthesis and characterization of ruthenium oxide nanosheets using polymer additive for supercapacitor applications. J Mater Sci Mater Electron 29:323–330
36. Kim SY, Shin WH, Kim H-S, Jung DW, Kim M-J, Kim K, Roh JW, Hwang S, Lee J, Yang D, Sohn H, Kim SH, Jung C, Cho E, Yun D-J, Kim J, Cho YJ, Kim S-I, Lee KH, Kwak C, Ko D-S (2021) Silver nanowire network hybridized with silver nanoparticle-anchored ruthenium oxide nanosheets for foldable transparent conductive electrodes. ACS Appl Mater Interfaces 13:11396–11402
37. Lee JM, Mok EK, Lee S, Lee N-S, Debbichi L, Kim H (2016) A conductive hybridization matrix of RuO_2 two-dimensional nanosheets: a hybrid-type photocatalyst. Angew Chem Int Ed 55:8546–8550
38. Laha S, Lee Y, Podjaski F, Weber D, Duppel V, Schoop LM, Pielnhofer F, Scheurer C, Müller K, Starke U, Reuter K, Lotsch BV (2019) Ruthenium oxide nanosheets for enhanced oxygen evolution catalysis in acidic medium. Adv Energy Mater 9:1803795
39. Zhao ZL, Wang Q, Huang X, Feng Q, Gu S, Zhang Z, Xu H, Zeng L, Gu M, Li H (2020) Boosting the oxygen evolution reaction using defect-rich ultra-thin ruthenium oxide nanosheets in acidic media. Energy Environ Sci 13:5143–5151
40. Morgan DJ (2015) Resolving ruthenium: XPS studies of common ruthenium materials. Surf Interface Anal 47:1072–1079
41. Wang C, Osada M, Ebina Y, Li B-W, Akatsuka K, Fukuda K, Sugimoto W, Ma R, Sasaki T (2014) All-nanosheet ultrathin capacitors assembled layer-by-layerviasolution-based processes. ACS Nano 8:2658–2666
42. Osada M, Sasaki T (2003) Exfoliated oxide nanosheets: new solution to nanoelectronics. J Mater Chem 19:2503–2511